RSC Advances

PAPER

Cite this: *RSC Adv.*, 2015, **5**, 22334

Au@UiO-66: a base free oxidation catalyst†

K. Leus,[a] P. Concepcion,[b] M. Vandichel,[c] M. Meledina,[d] A. Grirrane,[b] D. Esquivel,[a] S. Turner,[d] D. Poelman,[e] M. Waroquier,[c] V. Van Speybroeck,[c] G. Van Tendeloo,[d] H. García[b] and P. Van Der Voort*[a]

Received 21st December 2014
Accepted 19th February 2015

DOI: 10.1039/c4ra16800c

www.rsc.org/advances

We present the *in situ* synthesis of Au nanoparticles within the Zr based Metal Organic Framework, UiO-66. The resulting Au@UiO-66 materials were characterized by means of N_2 sorption, XRPD, UV-Vis, XRF, XPS and TEM analysis. The Au nanoparticles (NP) are homogeneously distributed along the UiO-66 host matrix when using $NaBH_4$ or H_2 as reducing agents. The Au@UiO-66 materials were evaluated as catalysts in the oxidation of benzyl alcohol and benzyl amine employing O_2 as oxidant. The Au@MOF materials exhibit a very high selectivity towards the ketone (up to 100%). Regenerability and stability tests demonstrate that the Au@UiO-66 catalyst can be recycled with a negligible loss of Au species and no loss of crystallinity. *In situ* IR measurements of UiO-66 and Au@UiO-66-$NaBH_4$, before and after treatment with alcohol, showed an increase in IR bands that can be assigned to a combination of physisorbed and chemisorbed alcohol species. This was confirmed by velocity power spectra obtained from the molecular dynamics simulations. Active peroxo and oxo species on Au could be visualized with Raman analysis.

1. Introduction

Since the breakthrough discovery by Haruta *et al.* on the use of Au nanoparticles (NP) for the low temperature aerobic oxidation of carbon monoxide many other aerobic oxidation reactions have been reported.[1,2] For instance gold NP have been used to catalyze the selective oxidation of hydrocarbons, sugars, carbonyl compounds, alcohols and in the oxidation of amines to amides.[3–6] Nevertheless, a severe problem in gold catalysis is their facile sintering and irreversible aggregation. To stabilize the gold NP many different supports have been examined as host materials. The most commonly employed support materials are metal-oxides *e.g.* CeO_2, TiO_2, Al_2O_3 [7–11] but also carbon and silica based materials have been extensively investigated.[12–18]

Alternatively, attempts have been made to synthesize NP inside Metal Organic Frameworks (MOFs), which is another efficient way to stabilize NP. MOFs are crystalline porous materials constructed from metal ions or metal clusters interconnected by rigid organic linkers. MOFs have been examined for many potential applications, for example in gas sorption and separation, sensing, luminescence and in catalysis.[19–21] In particular in the field of heterogeneous catalysis, there is an increasing interest towards embedding of NP in MOFs. Thus far, Pd, Ru, Cu, Pt, Ni, Ag and Au NP have been incorporated in MOFs.[22] The reported Au@MOF materials were often examined for the liquid phase oxidation of benzyl alcohol. However, different reaction conditions were used in the catalytic studies. First, there is a lot of debate on the question if a base is required. Müller *et al.* showed that if no base was added to the reaction mixture, the Au@MOF-5, Au/ZnO@MOF-5 and Au/TiO_2@MOF-5 catalyst showed no catalytic activity in the oxidation of benzyl alcohol, whereas in the presence of the base K_2CO_3, the oxidation reaction is accelerated by deprotonation of the alcohol.[23] Nonetheless, in the report of Liu *et al.* concerning Au@MIL-101, the Au@MOF material could efficiently catalyze the oxidation of alcohols under ambient conditions in the absence of a base.[24] The high dispersion of the Au NP and the electron donation effects of the aryl rings to the Au NP within the cages of the MIL-101 support have been put forward as the main reason for the high activity. It was suggested that the support may play a

[a]*Department of Inorganic and Physical Chemistry, Center for Ordered Materials, Organometallics and Catalysis (COMOC), Ghent University, Krijgslaan 281-S3, 9000 Ghent, Belgium. E-mail: pascal.VanDerVoort@ugent.be*

[b]*Instituto de Tecnología Química, CSIC-UPV, Universidad Politécnica de Valencia, Av. de los Naranjos s/n, 46022 Valencia, Spain*

[c]*Center for Molecular Modeling, Ghent University, Technologiepark 903, 9052 Zwijnaarde, Belgium*

[d]*Electron Microscopy for Materials Science (EMAT), University of Antwerp, Groenenborgerlaan 171, 2020 Antwerp, Belgium*

[e]*Department of Solid State Sciences, Lumilab, Ghent University, Krijgslaan 281-S1, 9000 Ghent, Belgium*

† Electronic supplementary information (ESI) available: XRPD patterns of the UiO-66 and the Au@UiO-66 materials, HAADF-STEM electron tomography reconstruction of the Au@UiO-66-H_2 material and IR spectra of pentanol adsorbed on the Au@UiO-66-$NaBH_4$ in the absence and presence of O_2. Plausible oxidation mechanisms on the Au nanoparticles. N_2 sorption isotherms of Au@UiO-66-$NaBH_4$ before and after catalysis and the conversion patterns of the first and second run. Details on the cluster calculations and molecular dynamics simulations. See DOI: 10.1039/c4ra16800c

crucial role, either direct or indirect, in the activity of gold.[25–28] The influence of the support was also illustrated in the work of Ishida *et al.* in which large differences in alcohol conversions were observed for the Au@MOF-5, Au@Al-MIL-53, and Au@$Cu_3(BTC)_2$.[29] Also in the work of Esken *et al.* it was suggested that the Au NP may chemically interact with the functionalities on the organic linker. They observed a remarkable difference in catalytic activity between Au@ZIF-8, which exhibits a high conversion (81%) of benzyl alcohol, whereas the Au@ZIF-90 shows a very weak activity (13%). The latter is due to *in situ* oxidation of the aldehyde functions of ZIF-90 by means of the Au NP imbedded in the MOF, making the active Au sites inaccessible for further reaction.[30] Very recently Zhu *et al.*[31] reported on the synthesis of Au@UiO-66 which was examined in the oxidation of benzyl alcohol in the presence of O_2 and a base. UiO-66 (UiO: University of Oslo) is a stable Zr-based MOF, first reported by Lillerud *et al.*[32] It is known that in the UiO-66 framework, terephthalate defects or missing linkers create accessible Zr-sites,[33] which are responsible for the catalytic activity.[34] Experimental techniques are developed to control the amount of open Zr-sites within the UiO-66 material.[35–37]

In this paper we report on the synthesis and characterization of Au NP in the cubic Zr terephthalate UiO-66 material. The resulting Au@UiO-66 material was tested for its catalytic activity in the oxidation of benzyl alcohol and benzyl amine using oxygen as the only oxidant.

2. Materials and methods

2.1 General procedures

All chemicals were purchased from Sigma Aldrich or TCI Europe and used without further purification. Nitrogen adsorption experiments were carried out at −196 °C using a Belsorp-mini II gas analyzer. Prior to analysis, the samples were dried under vacuum at 120 °C to remove adsorbed water. X-ray powder diffraction (XRPD) patterns were collected on a ARL X'TRA X-ray diffractometer with Cu Kα radiation of 0.15418 nm wavelength and a solid state detector. X-ray Fluorescence (XRF) measurements were performed on a NEX CG (Rigaku) using a Mo-X-ray source. UV-Vis measurements were carried out on a Varian Cary 500 dual beam UV-Vis-Near IR spectrophotometer, applying an internal 110 mm $BaSO_4$-coated integrating sphere. Elemental analyses of the leached species after catalysis were performed by inductively coupled plasma-optical emission spectroscopy (ICP-OES) on a Varian 715-ES. Prior to analysis, the catalytic mixture was evaporated to dryness and redissolved in an H_2SO_4 aqueous solution. Gas chromatography (GC) experiments were conducted on a Varian 3900 apparatus equipped with an TRB-5MS column (5% phenyl, 95% polymethylsiloxane, 30 m, 0.25 mm × 0.25 μm, Teknokroma) using He as carrier gas. The reaction products were identified with a GC/MS spectrometer (Agilent) equipped with the same column as the GC and operated under the same conditions. XPS spectra were recorded with a SPECS Phoibos HAS 3500 150 MCD. The X-ray source was, using a Mg anode ($h\nu = 1253.6$ eV), powered at 12 kV, 25 mA. The samples were pressed into pellets and introduced into the spectrometer without previous thermal treatment. They were outgassed overnight and analyzed at room temperature. Accurate binding energies (BE) were determined with respect to the position of the C 1s peak at 284.8 eV. The peaks were decomposed using a least-squares fitting routine (Casa XPS software) with a Gauss/Lorentz ratio of 70/30 and after subtraction of a Shirley background. HAADF-STEM imaging was carried out on an aberration-corrected FEI Titan "cubed" microscope, operated at 120 or 300 kV acceleration voltage, using a convergence semi-angle α of 22 mrad and an inner acceptance semi-angle β of 50 mrad at 300 kV and 85 mrad at 120 kV to ensure HAADF-STEM imaging conditions. EDX mapping was performed on the same instrument, using a large solid-angle Bruker "Super-X" EDX detector setup. Electron tomography was performed on a FEI Tecnai microscope, operated at 200 kV acceleration voltage under HAADF-STEM conditions. Images were acquired at 5 degree intervals, from −70 to +65 degrees. Tomographic reconstruction using a SIRT algorithm (20 iterations) was carried out using the FEI inspect3D software, the 3D visualization was made using the FEI AMIRA software package. FTIR spectra were recorded with a Bruker, Vertex70 spectrometer, by using a conventional quartz infrared cell connected to a vacuum dosing system. The catalyst powder was pressed into self-supporting wafers (5 mg) and activated at 150 °C in vacuum (10^{-5} mbar) for 1 h, before carrying out adsorption experiments. Because of the low vapour pressure of benzyl alcohol (which was used in the catalytic studies) pentanol was employed for the *in situ* IR studies. The test reaction was performed *ex situ* under similar catalytic conditions of the benzyl alcohol oxidation in order to assure aldehyde formation. The adsorption of pentanol was performed at 3 mbar and 25 °C, followed by increasing temperatures and/or co-adsorption of 15 mbar O_2. Raman spectra were recorded with a 785 nm laser excitation on a Renishaw Raman Spectrometer ("in via") equipped with a CCD detector. A Linkam catalytic cell allowing gas treatments at different reaction temperatures was employed. The laser power on the sample was 0.2 mW and a total of 20 acquisitions were taken for each spectrum. Spectra were recorded under a N_2 flow (20 mL min^{-1}) at 100 °C followed by an O_2 flow (20 mL min^{-1}) at the same temperature (100 °C).

2.2 Synthesis of UiO-66

The UiO-66 material was synthesized according to the recipe described by Biswas *et al.*[38] 0.31 mmol of $ZrO_2Cl_2 \cdot 8H_2O$ was mixed together with 0.31 mmol of benzene-1,4-dicarboxylic acid (BDC) in 1.2 mL formic acid and 3 mL dimethylacetamide. The resulting mixture was placed at 150 °C for 24 hours, filtered off and washed several times with aceton. The resulting UiO-66*as* was stirred in DMF for 12 hours and in methanol for 24 hours at room temperature to remove unreacted linker. Hereafter the sample was dried under vacuum at 65 °C for 24 hours prior to use.

2.3 Synthesis of Au@UiO-66

The Au@UiO-66 materials were obtained by mixing 0.15 g of UiO-66 with 7 mg of $HAuCl_4$ in 40 mL of MeOH. The resulting mixture was stirred at RT for 6 hours under a nitrogen atmosphere. Three different methods were examined to reduce the gold. In the first method, $NaBH_4$ was added (10 times excess) and stirred for an additional hour at RT before filtration; the resulting sample is denoted as Au@UiO-66-$NaBH_4$. In a second method, triethylamine (30 times excess) was added as reducing agent to the mixture and stirred for 1 hour at RT. In the following this sample will be referred to as Au@UiO-66-triethylamine. The samples obtained after reduction by triethylamine or $NaBH_4$ were washed thoroughly with MeOH to remove unreacted reducing agent. In a third method, the Au@UiO-66 was placed for 2 hours at 200 °C under a H_2/argon stream; the resulting sample is denoted as Au@UiO-66-H_2.

2.4 Catalytic setup

In each catalytic test 0.25 mmol of the substrate (benzyl alcohol or benzyl amine) was loaded in the reactor together with 1 mL of toluene (solvent) and 0.10 mmol of dodecane (used as internal standard). 2 mol% (0.005 mmol) of the catalyst was added to the reaction mixture before sealing the reactor and placing it under a pressure of 5 bar O_2. All the catalytic tests were performed at a temperature of 100 °C. The Au@UiO-66-$NaBH_4$ is used as catalyst, unless otherwise noted. During each test, aliquots were gradually taken out of the mixture, diluted with toluene and subsequently analyzed by GC-FID. All the fresh catalysts were activated under vacuum at 120 °C for 3 h prior to catalysis. Blank tests at 100 °C showed no conversion at all. Additionally catalytic tests were performed using the host material, UiO-66, as oxidation catalyst. No conversion of benzyl alcohol and benzyl amine was observed after 9.5 hours of reaction.

3. Characterization of the Au@UiO-66 materials

3.1 XRPD, nitrogen adsorption measurements and determination of the Au loading

The Au loading of each Au@UiO-66 material was determined by means of XRF (see Table 1). Approximately the same loading was obtained in each material, with an average of 0.1 mmol Au g^{-1}. Furthermore, the crystallinity of all the obtained Au@UiO-66 materials was verified by XRPD measurements (see Fig. S1 ESI†). The XRPD pattern of each Au@MOF material presents the pure phase of the non-functionalized UiO-66. This explicitly shows that the framework integrity of the parent MOF was well preserved during the *in situ* synthesis of the Au NP. Nitrogen sorption measurements were carried out to determine the Langmuir surface area of the Au@UiO-66 materials. The pristine UiO-66 material has a Langmuir surface area of approximately 1200 m^2 g^{-1} which corresponds to the reported value in literature.[38] After the synthesis of the Au NP no significant changes are observed in the Langmuir surface area for the Au@MOF materials reduced by means of $NaBH_4$ and H_2. The Au@UiO-66-$NaBH_4$ and Au@UiO-66-H_2 material has a surface area of respectively 1172 m^2 g^{-1} and 1193 m^2 g^{-1}. The material reduced by means of triethylamine, has a lower Langmuir surface area of 980 m^2 g^{-1}.

Table 1 Langmuir surface area and Au loading of the Au@UiO-66 materials

Sample	Au loading (mmol g^{-1})	S_{Lang} (m^2 g^{-1})
Au@UiO-66-$NaBH_4$	0.12	1172
Au@UiO-66-triethylamine	0.09	980
Au@UiO-66-H_2	0.10	1193

3.2 UV-Vis and XPS measurements

The Au NP in the UiO-66 materials were further investigated by means of UV-Vis diffuse reflectance spectroscopy measurements. In Fig. 1 the UV-Vis spectra are depicted of the Au@UiO-66 materials. A broad peak centered around 527 nm, characteristic for gold colloids, is observed in the Au@UiO-66 materials which is absent in the pristine UiO-66 material. The absorption edge at approximately 300 nm can be attributed to the matrix of the host material.[39]

To determine the valence state of the Au atoms in the Au@UiO-66 materials X-ray photoelectron spectroscopy measurements were carried out. The XPS spectrum of Au@UiO-66-$NaBH_4$ displays the Au 4f doublet (Au $4f_{7/2}$ at 83.9 eV and Au $4f_{5/2}$ at 87.5 eV) (Fig. 2). It can be deconvoluted in two pairs of doublets which can be ascribed to metallic Au and Au^{1+} species at 83.8 and 85.1 eV (Au $4f_{7/2}$) respectively. Fig. 2 also reveals that the Au@UiO-66-$NaBH_4$ material possesses a large amount of metal Au species and only a minor fraction of Au^{1+}. The surface concentration ratios of all the Au@UiO-66 materials are listed in Table 2. We examined different reduction methods, but systematically a similar amount of metallic Au species, approximately 88–95%, is measured, whereas only a small amount of Au^{1+} is observed (5–12%).

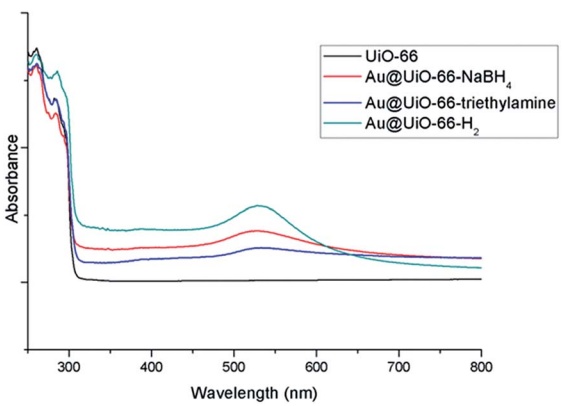

Fig. 1 UV-Vis spectra of the Au@UiO-66 materials.

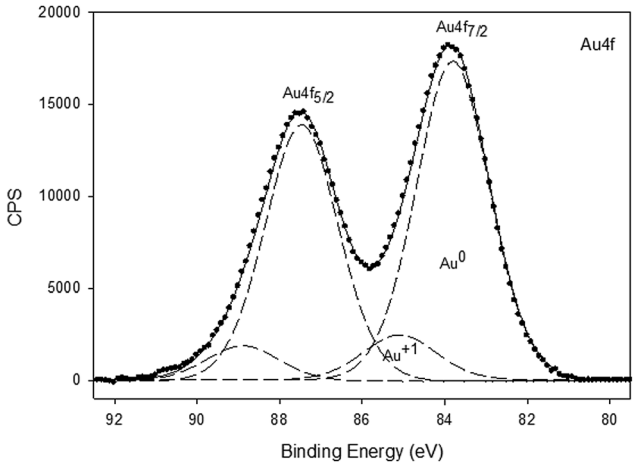

Fig. 2 XPS spectrum in the Au 4f region of Au@UiO-66-$NaBH_4$.

Table 2 Atomic concentration of the different valence states of the Au NP in the Au@UiO-66 materials

Sample	Au(0)/%	Au(I)/%
Au@UiO-66-$NaBH_4$	87.7	12.3
Au@UiO-66-triethylamine	95.3	4.7
Au@UiO-66-H_2	92.1	7.9

3.3 TEM measurements

To investigate the presence, size and distribution of the Au nanoparticles over the different Au@UiO-66 materials, we used high-angle annular dark field scanning transmission electron microscopy (HAADF-STEM/Z-contrast) imaging. The image contrast in HAADF-STEM images is known to be sensitive to both the atomic number $Z \sim 1.7$ as well as the sample thickness. Consequently the "heavy" Au NP present in the Au@UiO-66 materials display a strong image contrast. It is clear from the HAADF-STEM images in Fig. 3 that the Au NP sizes for all the Au@UiO-66 samples are similar, except for the Au@UiO-66-triethylamine material. In this sample, all the Au is clustered into larger structures, and is not dispersed as small Au nanoparticles. A detailed size distribution for the Au@UiO-66-$NaBH_4$ and Au@UiO-66-H_2 material is plotted in Fig. 3g. The average Au NP size for the Au@UiO-66-$NaBH_4$ is 7 nm ($\sigma = 4$ nm), whereas the average particle size for the Au@UiO-66-H_2 sample is 5 nm ($\sigma = 3$ nm). This implies that the size of the Au NP is much larger than the typical octahedral cage-dimensions of the UiO-66, which are smaller than 2 nm. This points to the presence of correlated defect nanoregions, which were also observed very recently in the UiO-66(Hf) material.[40] This type of large compositional defects is ideally suited for the Au NP incorporation. An energy-dispersive X-ray (EDX) chemical map taken from the sample Au@UiO-66-H_2 is displayed in Fig. 3e. From this figure, it is clear that the nanoparticles are pure Au, and are not covered by any type of non-Au shell. The nanoparticles are polycrystalline, as evidenced by the high resolution image

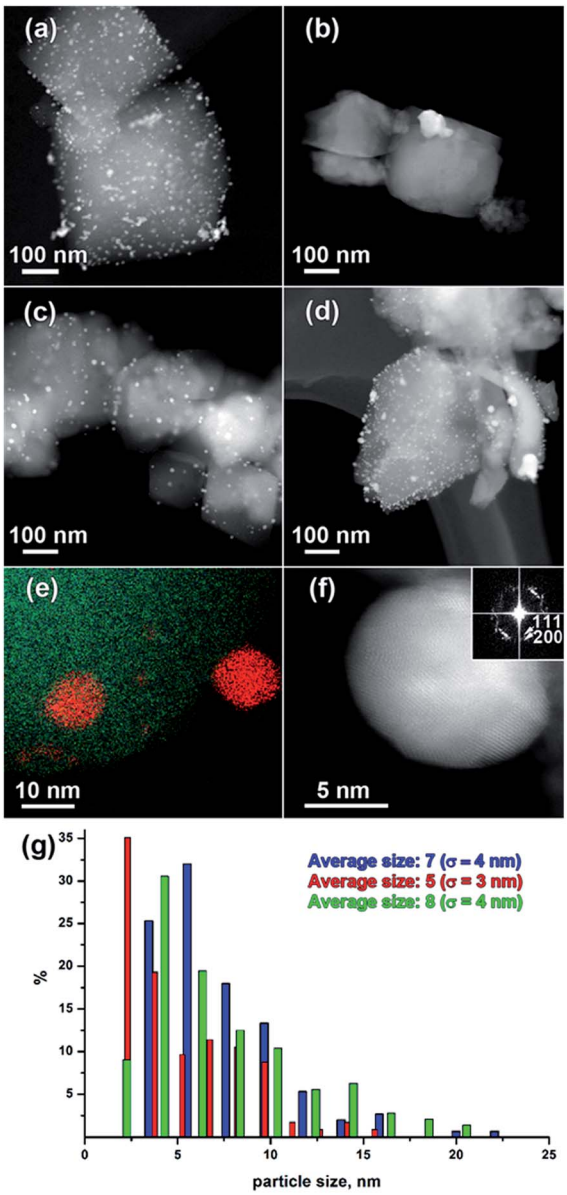

Fig. 3 (a–d) HAADF-STEM images of Au@UiO-66-$NaBH_4$ (a), Au@UiO-66-triethylamine (b), Au@UiO-66-H_2 (c) and Au@UiO-66-$NaBH_4$ after catalysis (d). (e) EDX chemical map of Au@UiO-66-H_2 with Zr mapped in Green, O in Blue and Au in Red. (f) High resolution HAADF-STEM image of a single polycrystalline Au NP in the Au@UiO-66-H_2 material with inset Fourier Transform pattern. (g) Size distributions for the Au NP in Au@UiO-66-$NaBH_4$ (Blue) in Au@UiO-66-H_2 (Red) and in Au@UiO-66-$NaBH_4$ after catalysis (Green).

in Fig. 3f. Unfortunately, the projected nature of the HAADF-STEM images in Fig. 3 does not allow to determine whether the Au nanoparticles in the Au@UiO-66 materials reduced by $NaBH_4$ or H_2 are evenly distributed throughout the UiO-66 framework host. In order to obtain this information, we performed an electron tomography reconstruction on the Au@UiO-66-H_2 sample (see Fig. S2† + movie showing the tomographic reconstruction of Au@UiO-66-H_2). The results clearly show that the Au NP in this sample are evenly distributed throughout the UiO-66 material, without

Table 3 Examined substrates using Au@UiO-66-$NaBH_4$ as catalyst

Substrate	Oxidant	Conversion (%)	Reaction time (hours)	Selectivity (%)
Benzyl alcohol	O_2	94	9.5	100
Benzyl alcohol	Air	83	23	100
Benzyl amine	O_2	53	24	100

preferential enrichment of the Au nanoparticles at the UiO-66 surface.

4. Catalytic performance

In Table 3, an overview is presented of the investigated substrates employing Au@UiO-66-$NaBH_4$ as catalyst. As can be seen from this table, the catalyst exhibits a good conversion for the oxidation of benzyl alcohol and benzyl amine. For the substrate benzyl amine a conversion of 53% was obtained after 24 hours of reaction with a selectivity of 100% towards *N*-benzyl-1-phenylmethanimine whereas for benzyl alcohol 94% of conversion was noted after 9.5 hours of catalysis with a selectivity of 100% towards benzaldehyde. Furthermore, the latter substrate can also be converted by air. By using 5 bar of air as oxidant 83% of benzyl alcohol was converted after 23 hours of reaction with the same selectivity.

Additionally, the Au@UiO-66-$NaBH_4$ material was compared with other Au@MOF based heterogeneous catalysts for the oxidation of benzyl alcohol. As can be seen from Table 4, all these Au based MOF catalysts, including the Au@UiO-66-$NaBH_4$, exhibit a good catalytic performance in the oxidation of benzyl alcohol. However, it is difficult to give an objective comparison, as different catalytic conditions were used in these tests. Nevertheless, it is clear that the solvent and the other catalytic conditions have a bigger influence on the selectivity and yield of the reaction than the actual type of MOF framework the gold nanoparticles are dispersed in. A high selectivity towards methyl benzoate is observed for the Au@MOF-5, Au@MIL-53, Au@ZIF-8, Au@ZIF-90 and Au/ZnO or Au/TiO_2@MOF-5 material (entry 1, 2 and 3) when the reaction is carried out with MeOH as solvent, whereas benzaldehyde is seen as the main product when no solvent, DMF or toluene is used (entry 1, 4, 5, 6, 7 and 8).

5. *In situ* IR measurements, Raman analysis and computational velocity power spectra

In the following, IR and Raman measurements, combined with molecular modeling techniques, have been performed to get more insight into plausible intermediates in the reaction mechanism. Due to the low vapour pressure of benzyl alcohol (which has been used in the catalytic studies), pentanol has been used for the *in situ* IR studies.

In Fig. 4 the IR spectrum of Au@UiO-66-$NaBH_4$ and UiO-66 is recorded before and after pentanol adsorption. Two ν(C–O) stretching vibrations[43] are observed at 1073 and 1052 cm^{-1} for both UiO-66 and Au@UiO-66-$NaBH_4$ (cfr. Fig. 4b and d), which point to the presence of similar adsorbed and chemisorbed species present in both samples. It should be noted that chemisorption of pentanol may result in Zr-pentoxide species (Scheme S2,† see section cluster calculations in ESI†) and

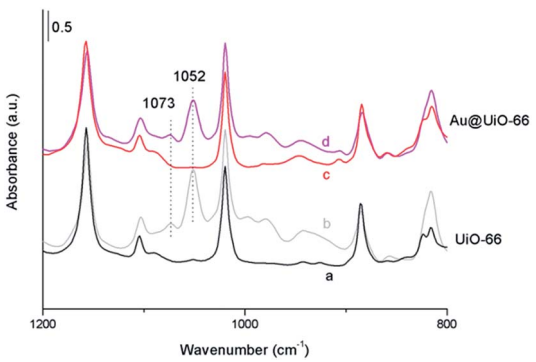

Fig. 4 IR spectra recorded at 25 °C on the UiO-66 sample before (a) and after 3 mbar pentanol adsorption (b) and on the Au@UiO-66-$NaBH_4$ sample before (c) and after 3 mbar pentanol adsorption (d).

Table 4 Comparison of the Au@UiO-66-$NaBH_4$ catalyst with other Au based MOF catalysts in the oxidation of benzyl alcohol

Entry	Catalytic MOF	Oxidant	Reaction conditions	Con-version (%)	Main product	Ref.
1	Au@MOF-5, Au@Al-MIL-53/ Au@Cu_3(BTC)$_2$	O_2	80 °C, MeOH + K_2CO_3 at 5 bar	70–98	Methyl benzoate/ benzaldehyde	29
2	Au@ZIF-8 and Au@ZIF-90	O_2	80 °C, 24 h in MeOH at 5 bar	13–81	Methyl benzoate (50–98%)	30
3	Au/ZnO@MOF-5 and Au/TiO_2@MOF-5	O_2	80 °C, 30 min in MeOH + K_2CO_3 at 5 bar	68–74	Methyl benzoate	23
4	Au@MIL-101	O_2 flow	80 °C, 1 atm, 1 h in toluene	>99	Benzaldehyde (>99%)	24
5	Au(1.5 wt%)/PMA-MIL-101	Air flow	80 °C, K_2CO_3, toluene at 353 K	60	Benzaldehyde (100%)	41
6	Au@UiO-66	O_2 flow	80 °C, K_2CO_3, 10 h	54	Benzaldehyde (100%)	31
7	Au@UiO-66-$NaBH_4$	O_2	100 °C, toluene, 5 bar, 9.5 h	94	Benzaldehyde (100%)	This work
8	Au@UiO-66-NH_2	O_2 flow	100 °C, 1 h DMF	94	Benzaldehyde	42

Au-pentoxide species. To obtain more insight into the nature of the adsorbed species both on the pristine UiO-66 and Au NP, first principle molecular dynamics calculations were performed on adsorbed pentanol and chemisorbed pentanol. To mimic the possible Zr-adsorption sites and Au-adsorption sites, we performed molecular dynamics calculations on a periodic UiO-66 model and on an Au NP of 54 Au atoms (construction of the models, see ESI†). As a near defect free UiO-66 sample can only be obtained at a synthesis temperature of 220 °C,[37] our employed synthesis temperature will result in a more defective UiO-66 host. Therefore, one BDC linker was removed in the calculations to create four accessible Zr-sites. Due to the large conformational flexibility of pentanol and various possible adsorption sites, molecular dynamics based calculations were proven to be essential to mimic the observed experimental vibrations. Adsorbed pentanol as well as pentoxide species were examined in both models during an MD run (NVT ensemble) at 25 °C. Subsequently, velocity power spectra (VPS) were constructed only from the velocities of the pentanol (or pentoxide) atoms. Rescaled VPS-spectra applying a scaling factor of 0.98 (Fig. 5b, c and e, f) were compared to the experimentally obtained difference spectra (Fig. 5a and d). First, we discuss the VPS spectra of pentanol and pentoxide species adsorbed on the Zr-sites of the parent UiO-66 material (Fig. 5a–c) and afterwards we will discuss the VPS spectra of such species on an Au NP (Fig. 5d–f).

As can be seen from Fig. 5a–c, the experimentally observed vibrations at 1052 cm^{-1} and 1073 cm^{-1} are also visible in the VPS spectra. Note that peak intensities in the VPS do not necessarily correspond with IR intensities, as these are dependent on the dipole moment of the vibrations, but the VPS peak positions could in principle be compared with experimental IR-peaks.[44] In the VPS-spectra, the band around 1052 cm^{-1} can be assigned to adsorbed pentanol species (on a Zr-site), while the band at around 1073 cm^{-1} can be associated to adsorbed pentanol as well as Zr-pentoxide species. Furthermore, the VPS bands around 815 cm^{-1} and 936 cm^{-1} might be fingerprints for the presence of Zr-pentoxide (Fig. 5c). Furthermore, we compared the theoretical VPS spectra obtained on an Au NP with the experimental difference spectrum between Au@UiO-66 samples before and after pentanol adsorption (Fig. 5d–f). In the Au@UiO-66 materials, both Au and Zr-sites are available for pentanol adsorption. The VPS spectra of Au-pentanol (Au-pentoxide) reveal clearly two bands at approximately 1050 and 1072 cm^{-1}, which were also present in the previous VPS spectra (Fig. 5b and c). Summarizing, in the experimental IR-spectrum of the pentanol treated Au@UiO-66 material (Fig. 4d), we cannot distinguish whether the bands originate from Zr-pentanol (Zr-pentoxide) or Au-pentanol (Au-pentoxide) species. Very probably, the experimental spectrum is an admixture of both signals.

In the IR-study, we could also clearly see that when pentanol was adsorbed on the Au@UiO-66-$NaBH_4$ material in the absence of O_2, no aldehyde was formed. In the presence of O_2, however, an additional vibration at 1714 cm^{-1} can be observed, assigned to the aldehyde species at a temperature of 100 °C (see Fig. S3†).

The computational results confirm that alcohol adsorption and even alkoxide formation reactions may take place on the Au NP, as was modelled in the recent work paper by Mullen *et al.*[45]

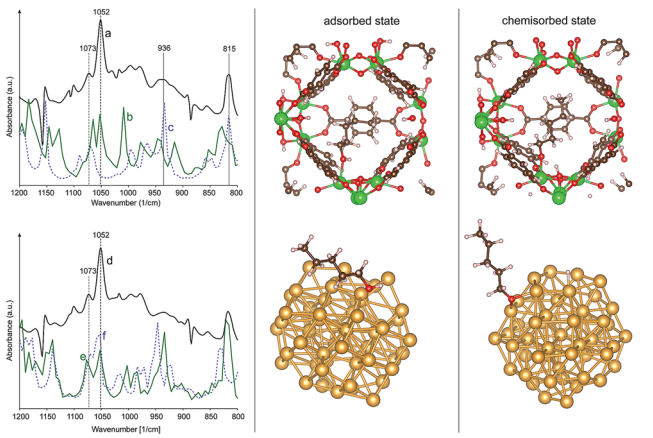

Fig. 5 (a) Difference spectrum between UiO-66 samples before and after 3 mbar pentanol adsorption recorded at 25 °C. Modeled velocity power spectra (VPS) of (b) adsorbed pentanol and (c) Zr-pentoxide species (scaling factor of 0.98), (d) difference spectrum between Au@UiO-66 samples before and after 3 mbar pentanol adsorption recorded at 25 °C. Modeled velocity power spectra (VPS) of (e) adsorbed pentanol at the Au NP and (f) Au-pentoxide species (scaling factor of 0.98). An adsorbed and chemisorbed state at the UiO-66 sample and Au NP are illustrated as occurring during the *ab initio* MD-simulations.

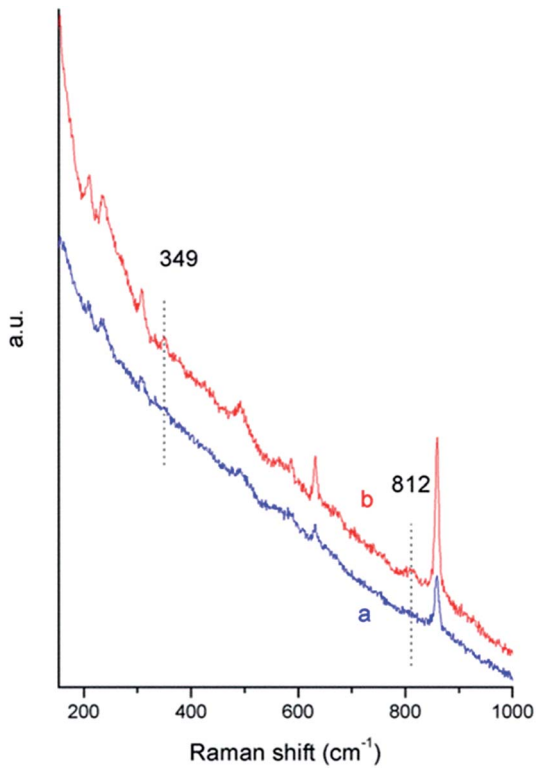

Fig. 6 Raman spectra of the Au@UiO-66-$NaBH_4$ sample in N_2 flow at 100 °C (a) and in O_2 flow at 100 °C (b).

However, these authors found that alkoxide formation from 2-propen-1-ol was highly activated without the presence of oxygen ad-atoms and surface hydroxyl species. In order to provide evidence for the formation of oxygen ad-atoms (Au–O) and peroxo species (Au–OO) during the catalytic tests, Raman measurements have been performed at 100 °C on the Au@UiO-66-$NaBH_4$ sample (Fig. 6). In the presence of O_2 new Raman bands appear at 349 cm^{-1} and 812 cm^{-1}, corresponding to the ν(Au–O) vibration and the ν(O–O) vibration respectively.[46] Summarizing, based on the observed spectra and the lack of any catalytic activity on the pure UiO-66, we can assume that Au plays an important role in the oxidation reaction with O_2. A detailed theoretical mechanistic study for the oxidation reaction on the Au nanoparticle is beyond the scope of the present article. However interesting features about plausible mechanisms can be found in literature. Inspired by a recent computational work of Mullen *et al.*[45] plausible reaction pathways are proposed in Scheme S1 (see ESI†). It has been shown by these authors that atomic oxygen and hydroxyl species, precovered on the Au surface, are active players in the allyl alcohol oxidation, each with a specific pathway of oxidation. The abstraction of the hydroxyl hydrogen of the allyl alcohol is initiated by either oxygen ad-atoms or adsorbed hydroxyl species on the gold surface. An allyl oxide is formed and it concerns an almost barrierless process following the calculations of Mullen *et al.*[45] These processes are schematically shown in Scheme S1b.† From Au-alkoxide, the second hydrogen abstraction is slightly higher activated with barriers amounting to 10.6 and 29.2 kJ mol^{-1} with surface oxygen and surface hydroxyl species respectively. Note that these results have been computed for an Au(111) surface, however, it is well known that the smaller the Au NP are, the higher the oxidation activity will be, and thus the lower the activation barriers are.[47]

6. Reusability and stability tests

To examine the regenerability of the Au@UiO-66-$NaBH_4$, an additional run was performed. In Fig. S4,† the first and second run is plotted using benzyl alcohol as substrate and in Table 5, the TON, TOF, selectivity and leaching percentage of each run is presented. An induction period is observed during the second run, which is probably due to the clogging of the pores. The latter observation was confirmed by nitrogen adsorption analysis (see Fig. S5†). The Langmuir surface area drops from 1172 $m^2\ g^{-1}$ to 865 $m^2\ g^{-1}$ after the first catalytic run. The TON and TOF values only decrease marginally in a second run. In a "high concentration" run, 2.5 mmol of benzyl alcohol was used instead of 0.25 mmol benzyl alcohol. As can be seen from Table 5, the TON number for the high concentration run is indeed almost 10 times higher. This observation demonstrates that the Au@UiO-66-$NaBH_4$ catalyst does not lose its activity during many turnovers. The TOF value is comparable, though slightly higher due to the increased initial substrate concentration. Additionally the selectivity of the catalyst stays unaltered during these additional runs and only a small amount of Au NP was leached out. More specifically, 0.66 and 0.18% of the Au species were leached out during the first two runs.

Comparison of the XRPD pattern of the Au@UiO-66-$NaBH_4$ before catalysis and after each run, shows that the framework integrity of the MOF is preserved after the second run (Fig. 7). Even after the high concentration run the crystalline structure of the host material was preserved. Additional proof for the stability of the Au@UiO-66-$NaBH_4$ was seen in the XPS and TEM measurements. From the TEM measurements (see Fig. 3g) no

Table 5 TON, TOF, selectivity and leaching percentage for each run using Au@UiO-66-$NaBH_4$ as catalyst

Run	TON	TOF (h^{-1})	Selectivity benzaldehyde (%)	Leaching Au (%)
Run 1	35[a]	7.5[b]	100	0.66
Run 2	28[a]	6[b]	100	0.18
High concentration run	330[c]	11.4[d]	100	1.9

[a] The TON number was determined after 9.5 hours of catalysis. [b] The TOF number was determined after 1.5 hours of catalysis. [c] The TON number was determined after 118 hours of catalysis. [d] The TOF number was determined after 3 hours of catalysis.

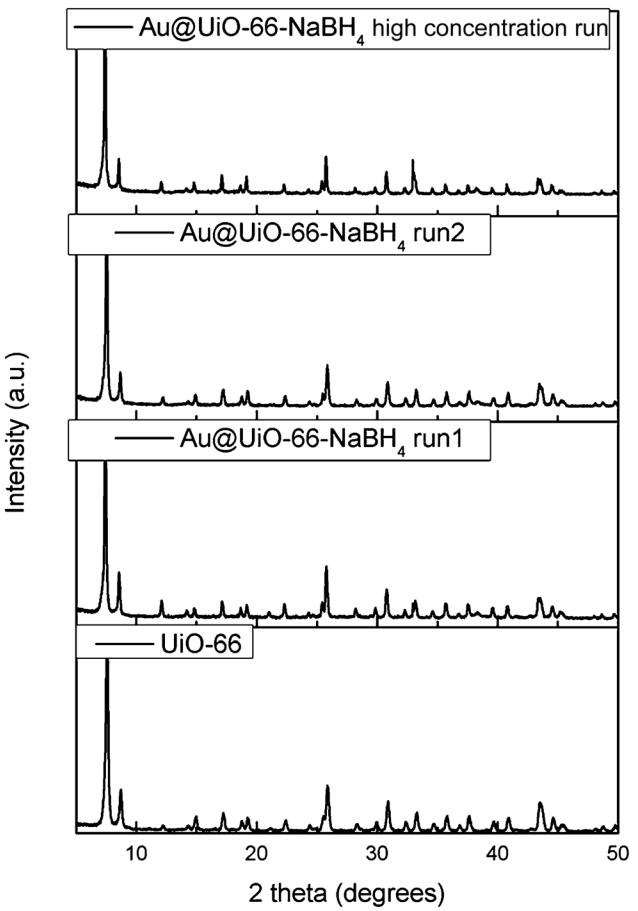

Fig. 7 XRPD pattern of Au@UiO-66-$NaBH_4$ before and after catalysis.

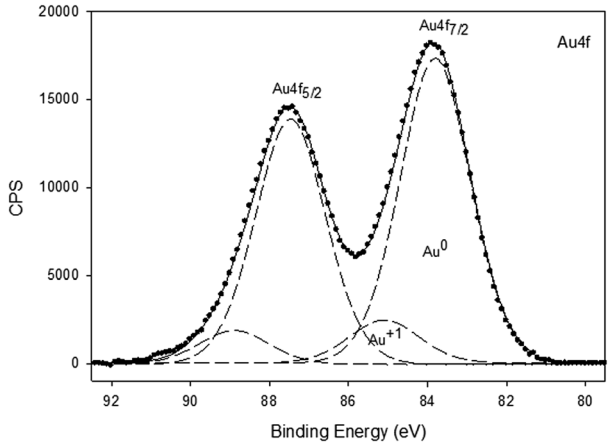

Fig. 8 XPS spectra in the Au 4f region of Au@UiO-66-$NaBH_4$ after catalysis.

significant change is observed in the Au NP size distribution before and after catalysis. The Au NP size after catalysis is approximately 8 nm ($\sigma = 4$ nm) whereas the size of the Au NP in the Au@UiO-66-$NaBH_4$ material before catalysis was 7 nm ($\sigma = 4$ nm). The Au 4f XPS spectrum of Au@UiO-66-$NaBH_4$ after catalysis showed two peaks at 83.9 and 87.5 eV assigned to Au $4f_{7/2}$ and Au $4f_{5/2}$, respectively (Fig. 8). After their deconvolution, an increase of the peak associated to Au^{1+} is observed, indicating a partial oxidation of the metallic Au to Au^{1+} species during the catalytic test.

7. Conclusions

Au NP were synthesized *in situ* within UiO-66. The Au NP were distributed homogeneously in the host material and no significant difference in the size distribution was observed based on the employed reduction method. The UiO-66 materials maintain their porosity and crystallinity during the synthesis of the Au NP and during the catalytic oxidation of benzyl alcohol. The Au@UiO-66 material is an efficient catalyst for the oxidation of benzyl alcohol using oxygen or air as oxidant and requires no additional base. The catalyst is 100% selective towards the ketone. In an effort to understand better the catalytic mechanism, we compared IR measurements on the pentanol treated Au@UiO-66 with the computationally obtained VPS spectra. The IR bands at 1050 and 1072 cm^{-1} can be assigned to Zr-pentanol (Zr-pentoxide) or Au-pentanol (Au-pentoxide) species and most probably to a combination of both. Moreover, Raman measurements showed the formation of oxygen ad-atoms (Au–O) and peroxo species (Au–OO) during catalysis, which play a crucial role in the hydrogen abstractions from alcohol and alkoxide species.

Acknowledgements

K.L. acknowledges the financial support from the Ghent University BOF postdoctoral grant 01P06813T and UGent GOA Grant 01G00710. M.V, S.T. and D.E. acknowledge funding from the Scientific Research-Foundation Flanders (FWO) for a postdoctoral fellowship. V.V.S. and M.W. acknowledge BELSPO in the frame of IAP-PAI P7/05. V.V.S. acknowledges funding from the European Research Council under the European Community's Seventh Framework Programme [FP7 (2007–2013) ERC grant agreement number 240483]. The computational resources and services used in this work were provided by VSC (Flemish Supercomputer Center), funded by the Hercules foundation and the Flemish Government – department EWI. This work was supported by funding from the European Research Council under the Seventh Framework Program (FP7), ERC grant no. 246791-COUNTATOMS.

Notes and references

1 M. Haruta, N. Yamada, T. Kobayashi and S. Iijima, *J. Catal.*, 1989, **115**, 301–309.
2 C. Della Pina, E. Falletta and M. Rossi, *Chem. Soc. Rev.*, 2012, **41**, 350–369.
3 Y. Zhu, H. F. Qian and R. C. Jin, *Chem.–Eur. J.*, 2010, **16**, 11455–11462.
4 A. Grirrane, A. Corma and H. Garcia, *J. Catal.*, 2009, **264**, 138–144.
5 O. Casanova, S. Iborra and A. Corma, *J. Catal.*, 2009, **265**, 109–116.
6 P. G. N. Mertens, S. L. F. Corthals, X. Ye, H. Poelman, P. A. Jacobs, B. F. Sels, I. F. J. Vankelecom and D. E. De Vos, *J. Mol. Catal. A: Chem.*, 2009, **313**, 14–21.
7 S. K. Klitgaard, A. T. DeLa Riva, S. Helveg, R. M. Werchmeister and C. H. Christensen, *Catal. Lett.*, 2008, **126**, 213–217.
8 S. Mandal, K. K. Bando, C. Santra, S. Maity, O. O. James, D. Mehta and B. Chowdhury, *Appl. Catal., A*, 2013, **452**, 94–104.
9 H. Wang, W. B. Fan, Y. He, J. G. Wang, J. N. Kondo and T. Tatsumi, *J. Catal.*, 2013, **299**, 10–19.
10 G. L. Hallett-Tapley, M. J. Silvero, C. J. Bueno-Alejo, M. Gonzalez-Bejar, C. D. McTiernan, M. Grenier, J. C. Netto-Ferreira and J. C. Scaiano, *J. Phys. Chem. C*, 2013, **117**, 12279–12288.
11 A. Tanaka, K. Hashimoto and H. Kominami, *J. Am. Chem. Soc.*, 2012, **134**, 14526–14533.
12 A. C. S. Sekhar, K. Sivaranjani, C. S. Gopinath and C. P. Vinod, *Catal. Today*, 2012, **198**, 92–97.
13 X. Wang, L. F. Chen, M. Shang, F. Lin, J. C. Hu and R. M. Richards, *Nanotechnology*, 2012, **23**, 294010.
14 C. Y. Ma, B. J. Dou, J. J. Li, J. Cheng, Q. Hu, Z. P. Hao and S. Z. Qiao, *Appl. Catal., B*, 2009, **92**, 202–208.
15 K. K. Zhu, J. C. Hu and R. Richards, *Catal. Lett.*, 2005, **100**, 195–199.
16 X. Q. Xie, J. L. Long, J. Xu, L. M. Chen, Y. Wang, Z. Z. Zhang and X. X. Wang, *RSC Adv.*, 2012, **2**, 12438–12446.
17 X. Q. Yu, Y. J. Huo, J. Yang, S. J. Chang, Y. S. Ma and W. X. Huang, *Appl. Surf. Sci.*, 2013, **280**, 450–455.
18 S. Wang, Q. F. Zhao, H. M. Wei, J. Q. Wang, M. Y. Cho, H. S. Cho, O. Terasaki and Y. Wan, *J. Am. Chem. Soc.*, 2013, **135**, 11849–11860.

19 K. Leus, Y. Y. Liu and P. Van Der Voort, *Catal. Rev.*, 2014, **56**, 1–56.
20 J. Heine and K. Muller-Buschbaum, *Chem. Soc. Rev.*, 2013, **42**, 9232–9242.
21 H. Furukawa, K. E. Cordova, M. O'Keeffe and O. M. Yaghi, *Science*, 2013, **341**, 974–987.
22 A. Dhakshinamoorthy and H. Garcia, *Chem. Soc. Rev.*, 2012, **41**, 5262–5284.
23 M. Müller, S. Turner, O. I. Lebedev, Y. M. Wang, G. van Tendeloo and R. A. Fischer, *Eur. J. Inorg. Chem.*, 2011, 1876–1887.
24 H. L. Liu, Y. L. Liu, Y. W. Li, Z. Y. Tang and H. F. Jiang, *J. Phys. Chem. C*, 2010, **114**, 13362–13369.
25 M. Boronat, P. Concepcion, A. Corma, S. Gonzalez, F. Illas and P. Serna, *J. Am. Chem. Soc.*, 2007, **129**, 16230–16237.
26 A. Corma and H. Garcia, *Chem. Soc. Rev.*, 2008, **37**, 2096–2126.
27 A. Abad, P. Concepcion, A. Corma and H. Garcia, *Angew. Chem., Int. Ed.*, 2005, **44**, 4066–4069.
28 A. Abad, A. Corma and H. Garcia, *Chem.–Eur. J.*, 2008, **14**, 212–222.
29 T. Ishida, M. Nagaoka, T. Akita and M. Haruta, *Chem.–Eur. J.*, 2008, **14**, 8456–8460.
30 D. Esken, S. Turner, O. I. Lebedev, G. Van Tendeloo and R. A. Fischer, *Chem. Mater.*, 2010, **22**, 6393–6401.
31 J. Zhu, P. C. Wang and M. Lu, *Appl. Catal., A*, 2014, **477**, 125–131.
32 J. H. Cavka, S. Jakobsen, U. Olsbye, N. Guillou, C. Lamberti, S. Bordiga and K. P. Lillerud, *J. Am. Chem. Soc.*, 2008, **130**, 13850–13851.
33 L. Valenzano, B. Civalleri, S. Chavan, S. Bordiga, M. H. Nilsen, S. Jakobsen, K. P. Lillerud and C. Lamberti, *Chem. Mater.*, 2011, **23**, 1700–1718.
34 F. Vermoortele, M. Vandichel, B. Van de Voorde, R. Ameloot, M. Waroquier, V. Van Speybroeck and D. E. De Vos, *Angew. Chem., Int. Ed.*, 2012, **51**, 4887–4890.
35 F. Vermoortele, B. Bueken, G. Le Bars, B. Van de Voorde, M. Vandichel, K. Houthoofd, A. Vimont, M. Daturi, M. Waroquier, V. Van Speybroeck, C. Kirschhock and D. E. De Vos, *J. Am. Chem. Soc.*, 2013, **135**, 11465–11468.
36 M. Vandichel, J. Hajek, F. Vermoortele, D. E. De Vos, M. Waroquier and V. Van Speybroeck, *CrystEngComm*, 2015, **17**(2), 395–406.
37 G. C. Shearer, S. Chavan, J. Ethiraj, J. G. Vitillo, S. Svelle, U. Olsbye, C. Lamberti, S. Bordiga and K. P. Lillerud, *Chem. Mater.*, 2014, **26**, 4068–4071.
38 S. Biswas and P. Van der Voort, *Eur. J. Inorg. Chem.*, 2013, 2154–2160.
39 H. R. Sahu and G. R. Rao, *Mater. Sci.*, 2000, **23**, 349–354.
40 M. J. Cliffe, W. Wan, X. D. Zou, P. A. Chater, A. K. Kleppe, M. G. Tucker, H. Wilhelm, N. P. Funnell, F. X. Coudert and A. L. Goodwin, *Nat. Commun.*, 2014, **5**, 1–8.
41 J. Juan-Alcaniz, J. Ferrando-Soria, I. Luz, P. Serra-Crespo, E. Skupien, V. P. Santos, E. Pardo, F. X. L. I. Xamena, F. Kapteijn and J. Gascon, *J. Catal.*, 2013, **307**, 295–304.
42 Y. Luan, Y. Qi, H. Y. Gao, N. N. Zheng and G. Wang, *J. Mater. Chem. A*, 2014, **2**, 20588–20596.
43 B. Stuart, *Infrared spectroscopy: fundamentals and applications*, John Wiley & Sons, 2004.
44 M. Van Houteghem, A. Ghysels, T. Verstraelen, W. Poelmans, M. Waroquier and V. Van Speybroeck, *J. Phys. Chem. B*, 2014, **118**, 2451–2470.
45 G. M. Mullen, L. Zhang, E. J. Evans, T. Yan, G. Henkelman and C. B. Mullins, *J. Am. Chem. Soc.*, 2014, **136**, 6489–6498.
46 P. Lakshmanan, L. Delannoy, C. Louis, N. Bion and J. M. Tatibouet, *Catal. Sci. Technol.*, 2013, **3**, 2918–2925.
47 B. Hvolbaek, T. V. W. Janssens, B. S. Clausen, H. Falsig, C. H. Christensen and J. K. Norskov, *Nano Today*, 2007, **2**, 14–18.